

Cite this: *Soft Matter*, 2011, **7**, 2552

www.rsc.org/softmatter

PAPER

# From craquelures to spiral crack patterns: influence of layer thickness on the crack patterns induced by desiccation

V. Lazarus<sup>a</sup> and L. Pauchard<sup>\*b</sup>

Received 31st August 2010, Accepted 22nd December 2010

DOI: 10.1039/c0sm00900h

As a film of dispersed colloidal particles consolidates by desiccation on a rigid substrate, enormous stresses develop. Most of the time, these stresses exceed the strength of the material causing crack formation. Although undesirable in most industrial cases, crack patterns exhibit a useful method to characterize paintings. Indeed, crack patterns are the signature of the particles, solvent and substrate type, the drying conditions and the film thickness. Here we focus on the influence of this last parameter on the final crack morphologies. In particular, using a colloidal dispersion with transparency properties, we observe that craquelures, delamination and spiral crack morphologies can be obtained by changing only the film thickness. An extensive description of the formation dynamics and final geometry of each pattern is presented, highlighting the key geometric parameters that may easily be used by a broad audience, including the mechanical engineering, physics, chemistry, geology and art communities.

## 1 Introduction

Coatings can be made by depositing a film of dispersed colloidal particles or dissolved macromolecules on a substrate and then by evaporating the solvent until a dry film forms. During the drying process, stresses appear in the film. If these stresses exceed the strength of the material, undesirable effects occur such as the formation of cracks with various morphologies ranging from craquelures to delamination or spiral patterns (Fig. 1). They occur in coatings, paintings and geological materials such as mud and should mostly be avoided in industrial fields for instance, in micro-electro-mechanical systems (MEMS). Although numerous experiments and models have been proposed for cracking during drying,<sup>1</sup> there is little consensus on even the most basic underlying mechanisms. Thus, a precise description of those patterns is of utmost importance. This paper aims to contribute to this description. It has theoretical significance in mechanics, physics and the chemistry of materials to understand the underlying mechanisms. It may also have practical significance, to help to understand by inverse method their formation conditions, for instance in engineering fields for expert evaluation after an accident, in geological fields for mud cracks<sup>2</sup> or septarias,<sup>3</sup> in the arts to study painter techniques<sup>4</sup> or to authenticate paintings.<sup>5-7</sup>

The resulting crack patterns depend notably on the type of the particles (size,<sup>8</sup> chemical composition<sup>9,10</sup>), the solvent and the

substrate, the drying conditions (temperature,<sup>11</sup> RH,<sup>12</sup> air velocity<sup>13</sup>) and the film thickness.<sup>14-16</sup> We focus here on the effect of the film thickness.

It is well known that below a critical thickness the film is free of cracks.<sup>12,14,17,18</sup> Above this critical thickness, mud cracks or craquelures appear. The nucleation of those cracks has been seldom studied.<sup>19</sup> When cracks divide the plane into polygonal adjacent cells, the cell size has extensively been described as a function of the thickness in various systems.<sup>14-16</sup> More recently, it has been noticed<sup>20</sup> that those polygonal mud cracks may be followed later on by delamination of the film from the substrate. In this way, a hard nanolatex bead dispersion exhibiting transparency in the dry phase has been used to follow the delamination process. Spiral cracks following the delamination front have been observed in drying precipitates.<sup>21</sup> Here, we consider the drying process of a dispersion chosen for its transparency. Changing only the film thickness, spiral cracks besides crack free films, mud cracks and delamination are observed. The spiral cracks are different from those previously observed<sup>21</sup> since they do not form until after the end of the delamination process. We perform an extensive description of the dynamics and geometry of those patterns, especially the case of the spiral cracks. Coupling crack morphologies and mass variations with time measurements, the key parameters are highlighted.

## 2 Materials and methods

### 2.1 Materials

We used aqueous dispersions of Latex particles provided by Rhodia Recherche, Aubervilliers, France. The particles are of

<sup>a</sup>UPMC Univ Paris 6, UMR 7608, Lab FAST, Bat 502, Campus Univ, F-91405 Orsay, France, EU. E-mail: lazarus@fast.u-psud.fr; Fax: +33 1 69 15 80 60; Tel: +33 1 69 15 80 39

<sup>b</sup>CNRS, UMR 7608, Lab FAST, Bat 502, Campus Univ, F-91405 Orsay, France, EU. E-mail: pauchard@fast.u-psud.fr; Fax: +33 1 69 15 80 60; Tel: +33 1 69 15 80 49

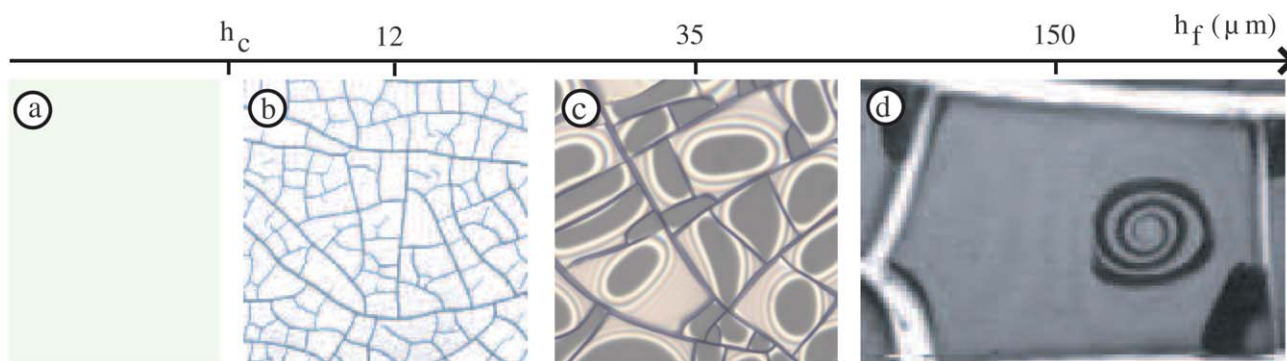


**Fig. 1** Crack patterns at the final stage of the drying process for different layer thicknesses,  $h_f$  (image height  $\sim 400 \mu\text{m}$ ). Uniform layer (a), cracks in the film thickness (b), delamination (c), spiral crack (d).

$2a = 30 \text{ nm}$  diameter and stabilized by surfactants (SDS);<sup>22</sup> also particles are polydisperse enough not to crystallize. The density of the particles is  $\rho_p = 1.08 \pm 0.02 \text{ g cm}^{-3}$ . At room temperature, since the glass transition temperature is  $100 \text{ }^\circ\text{C}$ , the particles are hard. The particles' volume fraction is high (initially  $\phi_0 = 25\%$ ) and the dispersion is stable in the absence of solvent evaporation. At the beginning of the drying process, the dispersion behaves as a liquid with a viscosity of  $\eta = 7 \text{ mPa s}$  (measurement done with a Contraves LS30 rheometer). The surface tension of the dispersion was measured by the Wilhelmy plate method and displays a value of  $\gamma = 61 \pm 5 \text{ mN m}^{-1}$ . At the final stage of the drying process, the colloidal gel is still transparent allowing the easy observation of the dynamics of crack patterns in the layer.

## 2.2 Setup and methods

Experiments are performed on films of various thicknesses that dry at room temperature under controlled relative humidity (RH  $\sim 50\%$ ) inside a glovebox. In this way, the desiccation takes place in the absence of convection in the vapor so that the evaporation is limited by diffusion of the solvent into the air.

Isotropic and uniform drying is obtained by two different methods depending on the film's thickness. The initial and final thicknesses at the center of the layer are denoted  $h_0$  and  $h_f$  respectively. For thick films ( $h_f > 10 \mu\text{m}$ ), a circular container (diameter  $\sim 20 \text{ mm}$ , height  $\sim 0.5 \text{ mm}$ ) is filled with a given amount of dispersion (Fig. 2a). The contact line of the dispersion is quenched at the upper edge of the wall (altuglas) and remains pinned all along the drying process. At the final stage we obtain a layer of approximately constant thickness in the center of the container. In this region, covering about 70% of the total surface area, the evaporation is isotropic and uniform. However, it is difficult to obtain uniform films using this method for lower thickness layers, typically  $h_f < 10 \mu\text{m}$ . In this range, a quantity of solution is scraped in a thin layer using two spacers with a known thickness (Fig. 2b). This yields liquid layers with final thickness  $h_f$  varying between  $3 \mu\text{m}$  and  $10 \mu\text{m}$  depending on the spacer thickness.

In both cases, the substrate is a nonporous glass plate, carefully cleaned with pure water then ethanol before being dried in a heat chamber at  $100 \text{ }^\circ\text{C}$ .

The final crack patterns are observed by optical microscopy. Differential focusing allows us to localize the cracks in the layer

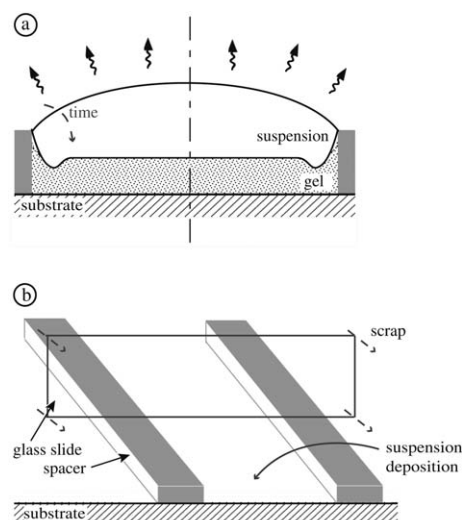


**Fig. 2** Experimental setups. (a) For thick layers (typically  $h_f > 10 \mu\text{m}$ ) a quantity of dispersion is deposited in a circular container and left to dry from the free surface. (b) For thin layers (typically  $h_f < 10 \mu\text{m}$ ) the setup consists in scraping a quantity of dispersion leaving a controlled thickness layer.

thickness. The final film thickness,  $h_f$ , is measured by successively focusing on the top (air–layer interface) and bottom (layer–substrate interface) of the deposited film in transmitted light. The accuracy of this method is to within  $3 \mu\text{m}$ .

The drying kinetics is obtained using a balance (Sartorius) with a precision of  $0.01 \text{ mg}$ . The drying rate is deduced from mass loss versus time (Fig. 3).

Simultaneously, the crack patterns formation is recorded using an interval timer, far from the boundaries of the sample, with a Leica camera positioned on the top of the sample.

## 3 Consolidation of the gel

### 3.1 Drying process

The drying process of a colloidal dispersion is usually<sup>23–25</sup> separated into two different stages, that can be roughly distinguished by measuring mass variations of the system with time (Fig. 3):

1. Initially a *constant rate period* (CRP) takes place during solvent evaporation; the evaporation rate is constant, close to the

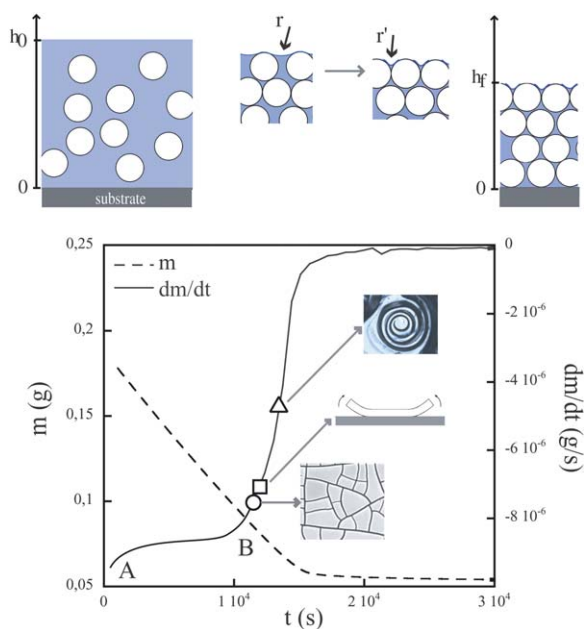


**Fig. 3** Top: schematic representation of the investigated dispersion of particles during the drying process. Left: dispersion ( $h_0$  denotes the thickness of the layer just after its deposition). Right: porous matrix saturated by solvent: curvature of the solvent–air menisci occurs at the evaporation surface during solvent loss ( $h_f$  is the value when the matrix does not pack any more). Graph: the sample mass,  $m$ , measured during the drying process is plotted *versus* time; the mass variations with time,  $dm/dt$ , is calculated from the mass measurements; (A) liquid state, evaporation at constant rate; (B) liquid–solid transition, formation of menisci at the liquid/air interface. Channelling cracks (O), delamination (□) and spiral cracks (△) are successively formed. Duration  $t_{CRP}$  extends between (A) and (B). Here  $h_0 = 580 \mu\text{m}$  and  $h_f = 220 \mu\text{m}$  (measurements in the middle of the circular container).

evaporation rate of pure solvent, and hence mainly controlled by the external conditions of relative humidity and temperature in the surroundings. During this stage, the surface of the gel remains saturated with solvent even if the solvent loss concentrates the dispersion as particles approach each other. The duration,  $t_{CRP}$ , of this stage depends on the initial volume fraction of the solvent in the dispersion, and also on the film thickness (Fig. 3).

2. This first stage is then followed by a non-linear drying rate period, namely the *falling rate period* (FRP), when the drying rate decreases with time (Fig. 3). During this second stage, the gel consolidates. As the liquid progressively recedes into the porous medium,<sup>25</sup> it forms at first menisci at the air/solvent interface due to capillary tension between the particles and then causes liquid bridges between the particles.

### 3.2 Tensile stresses and crack formation

During solvent evaporation curvature of the solvent–air menisci is responsible for a capillary pressure,  $P_{cap}$ , in the liquid phase. The maximum capillary pressure in the gel can reach  $P_{cap} = \frac{\alpha\gamma_{s,a}\cos(\theta)}{r_p}$ , where  $\gamma_{s,a}$  is the solvent–air surface tension,  $\theta$  the liquid/solid contact angle,  $r_p$  the pore radius ( $r_p \sim a$ ) and  $\alpha$  is a geometrical constant with a value of approximately<sup>9,24</sup> 10. This

depression induces shrinkage of the porous matrix that is constrained by the adhesion to the rigid substrate. Consequently high tensile stresses develops in the film.

As these tensile stresses progressively build up in the layer, the solid matrix consolidates and cracks appear in the film. The patterns depend on the layer thickness. At one extreme, below a critical film thickness  $h_C$ , the film is uniform and free of cracks at the end of the drying process (see also ref. 15, 16 for other systems). At the other extreme, above a critical film thickness  $h_S$ , a wealth of different patterns appear during the drying process (Fig. 4):

1. First, a *network of channelling cracks* appears hierarchically. The cracks are formed successively as described by the sequence in Fig. 4(a,b,c), dividing the plane into polygonal adjacent cells.<sup>26</sup>
2. During the end of channelling crack formation, another mode of crack formation takes place leading to the progressive detachment, that is *delamination*, of the layer from the substrate. A delaminating front nucleates from the limits of the polygonal cells and propagates as described in the sequence Fig. 4(a',b',c').
3. Finally, far after the delamination process *circular or spiral cracks* form in the adhering region of the layer with the substrate. Fig. 4(a'',b'',c'') display a series of images taken during the propagation of a conical spiral crack.

Between these two extremes:

1. For  $h_C < h_f < h_D$ , cracks in the layer form a partial or complete connected network, also called craquelures or mud cracks, but no delamination takes place.
2. For slightly thicker layers,  $h_D < h_f < h_S$ , hierarchical crack pattern and delamination but no spiral or circular cracks appear.

Whereas channelling cracks and delamination appear at the beginning of the FRP, the appearance of spiral or circular cracks is delayed some time after the end of the delamination process (Fig. 3). The times  $t_C$ ,  $t_D$ ,  $t_S$  of formation of channelling, delamination and spiral cracks (respectively) increase with the film thickness (Fig. 5).

Since the formation dynamics of the cracks depends on the film thickness, the final dried film contains (Fig. 1):

- for  $h_f < h_C$ , no cracks;
- for  $h_C < h_f < h_D$ , cracks in the film but no delamination;
- for  $h_D < h_f < h_S$ , cracks in the film and delamination cracks but no spiral or circular cracks;
- for  $h_f > h_S$ , cracks in the film, delamination then spiral or circular cracks.

This introduces the critical thicknesses  $h_C$ ,  $h_D$ , and  $h_S$ . We emphasize that they are material and drying conditions dependent and may serve to simply characterize the drying of any dispersion. In our modeled system we obtain:

$$h_C < 3 \mu\text{m}, h_D = 30 \pm 5 \mu\text{m}, h_S = 100 \pm 30 \mu\text{m}$$

The next section is devoted to a more precise description of each of the patterns.

## 4 Crack patterns

### 4.1 Craquelures ( $h_C < h_f$ )

Focusing more closely on the crack patterns that appear in the film thickness, one can distinguish for increasing thickness either

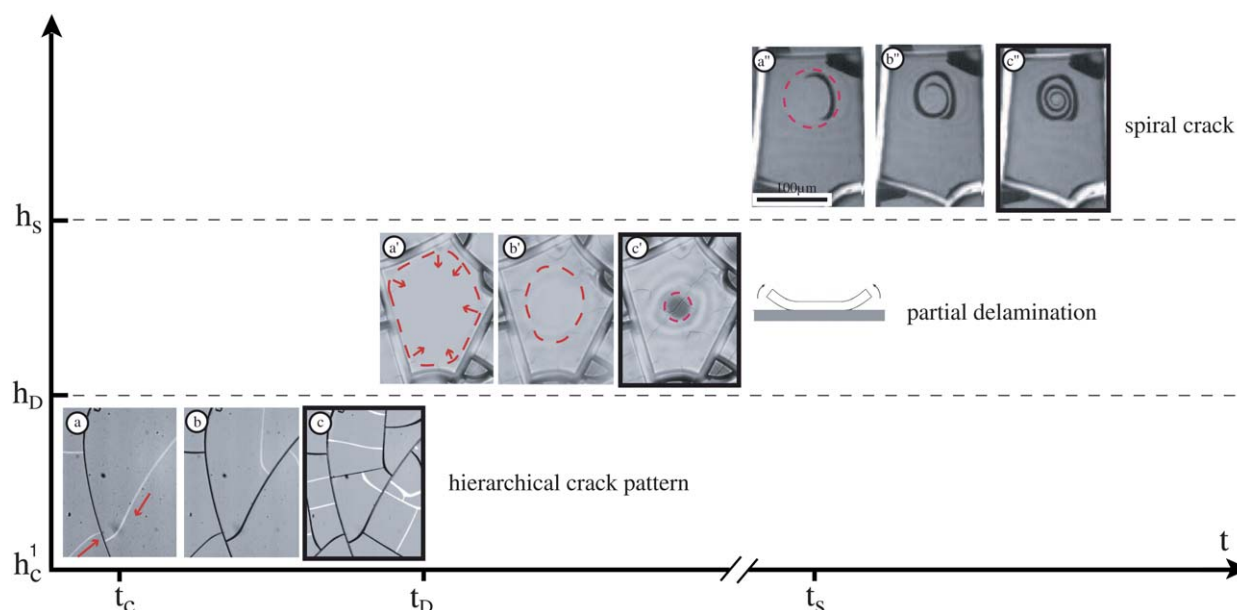


**Fig. 4** Formation of crack patterns for increasing film thicknesses. Images bordered by black frame correspond to the final pattern of each process. (a,b,c) Cracks in the thickness ( $h_C < h_f < h_D$ ): series of images showing hierarchical crack network formation (cracks of higher order are drawn in white). Delamination process takes place at a film thickness denoted by  $h_D$ . (a',b',c') Delamination process ( $h_D < h_f < h_S$ ). The delamination front is marked by a dashed line at different times. (a'',b'',c'') The sequence shows a spiral crack path formation ( $h_S < h_f$ ) (the adhering region is indicated by the dashed circle in (a'')).

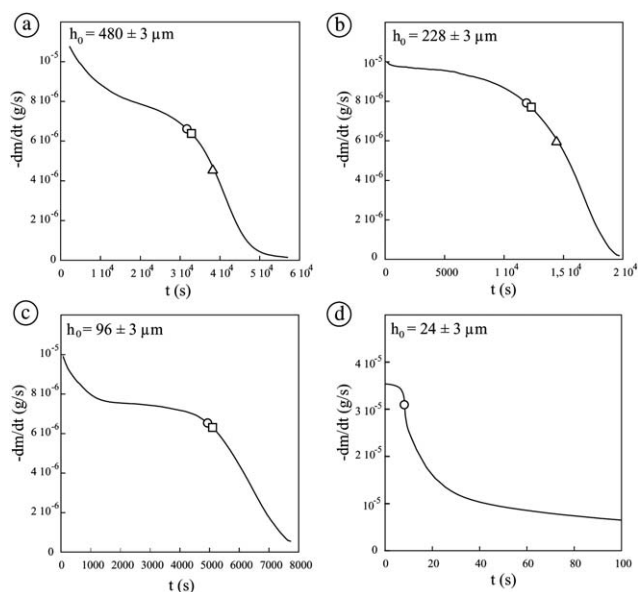


**Fig. 5** (a,b,c,d) Mass variations with time,  $dm/dt$ , during the drying process of layers of different initial thickness  $h_0$ . Channelling cracks (○), delamination (□) and spiral cracks (△) are successively formed, respectively at  $t_C$ ,  $t_D$  and  $t_S$ .

isolated junctions, sinuous cracks, or partially or complete connected network (Fig. 6a,b,c,d respectively). These patterns can be gathered into two main groups depending on the crack dynamics of propagation:

- for  $h_C < h_f < h_C^1$ , isolated junctions or sinuous cracks that are formed by *stable propagation* of the cracks as the loading increases (Fig. 6a,b);

- for  $h_C^1 < h_f$ , channelling cracks *unstably* propagate until they reach the cell boundary forming a partially or complete connected network (Fig. 6c,d).

Also a new critical thickness,  $h_C^1$ , is introduced. Here,

$$h_C^1 = 6 \pm 2 \mu\text{m}.$$

These two different crack patterns are described in the following subsections.

**Junctions and sinuous cracks ( $h_C < h_f < h_C^1$ ).** Above  $h_C$  and below  $h_C^1$ , a nucleation process takes place and the cracks propagate slowly as the loading increases during the drying process. For the thinner films, the cracks growth stops shortly after their initiation (Fig. 6a). Consequently two or three crack segments that are centered around the nucleation sites form isolated star like patterns. The crack density is low and depends on the distribution of nucleation sites (defects) in the layer.<sup>15,19</sup> For slightly thicker layers, cracks may propagate slowly as the loading increases forming sinuous cracks far from each other (Fig. 6b).

**Connected network ( $h_f > h_C^1$ ).** If  $h_f > h_C^1$ , as soon as a crack nucleates, it propagates unstably until it meets the boundary of the cell. This process takes place hierarchically: the cracks are formed successively as described by the sequence in Fig. 4(a,b,c). The first generation of cracks crosses the specimen. The next generations evolves in the mechanical stress field of the gelled layer modified by the existence of former cracks.<sup>26,27</sup> This situation results in a strong interaction that changes the local distribution of stresses. Also, the existing cracks define the boundary conditions for the mechanical stress field that governs the formation of future cracks: the stress components normal to the

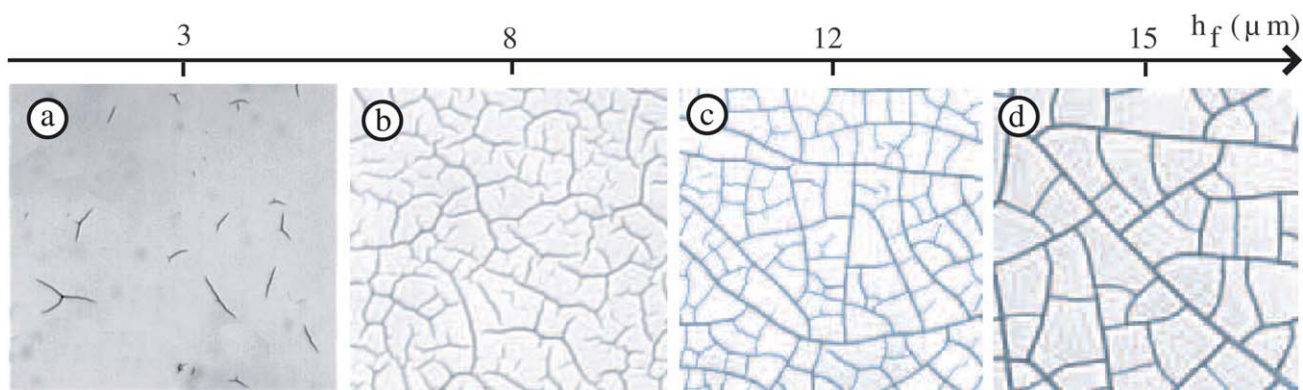


**Fig. 6** Example of final crack pattern showing broken or complete networks: isolated junctions (a), sinuous cracks (b), partially connected network (c) and complete connected network (d).

former crack direction are relaxed. When in this stress–relaxation zone, the propagating crack tilts progressively until it grows in a direction normal to the maximum tensile stress at the crack tip. Then the new crack intercepts the former one at a right angle.

The crack tilting due to the presence of a former crack path has been quantified by measuring the length,  $\beta$ , characterizing the direction changes for different layers (Fig. 7a). This length appears to be linearly dependent on the layer thickness (Fig. 7a). Here  $\alpha_0 \equiv \beta/h_f \sim 0.88$ .

During this process  $n$  generations of cracks appear. This number increases with the layer thickness.<sup>26</sup> In Fig. 6c,  $h_f \sim 12 \mu\text{m}$ , there are 4 generations of cracks and the cracks of order 4 does not connect to the previous ones leading to open branched structures: the last cracks to nucleate fail to cross the polygon sides formed by their older neighbors and remain open ended. Thus a partial broken network is formed. In a slightly thicker layer ( $h_f \sim 15 \mu\text{m}$ , Fig. 6d), cracks of order 4 four are connected to cracks of order 3 so generating closed cells, that form a complete connected network.

In the region of uniform drying process, the resulting crack pattern has no preferred orientation. In the case of a complete connected network (Fig. 6d), the characteristic length of the final pattern (polygonal cell size) scales with the layer thickness (Fig. 7b). The coefficient of proportionality  $\alpha_1 \equiv \sqrt{A_{\text{cell}}/h_f}$  ( $A_{\text{cell}}$  is the area of the cell) depends on the material and the drying conditions. For our dispersion,  $\alpha_1 = 42$  for RH = 50% and  $\alpha_1 = 50$  for RH = 70% (see ref. 20). For the ceria sol used by Atkinson and Guppy,<sup>14</sup> its value is  $\alpha_1 \sim 11.5$ . For the clay used by Colina and Roux,<sup>16</sup>  $\alpha_1 \sim 2.9$ . For the coffee–water mixture used by Groisman and Kaplan,<sup>15</sup>  $\alpha_1 \sim 4.2$ .

During the formation of the network of channelling cracks, the mechanical stresses are relieved by cracking. Also, the elastic energy stored in the layer decreases as and when space-dividing takes place. This situation limits the number of crack generations. However, for thicker layers, another process can limit the number of crack generations: the delamination process resulting in a detachment of the layer.

#### 4.2 Delamination ( $h_f > h_D$ )

As desiccation persists, stresses becomes high enough to continue the cracking process by the detachment of the gel from the

substrate. We clearly observe a delaminating front that nucleates from the corners of the polygonal cells and propagates inwards as described in the sequence Fig. 4b(a',b',c'). This results in shapes as shown in Fig. 8. At the final stage, each cell adheres to

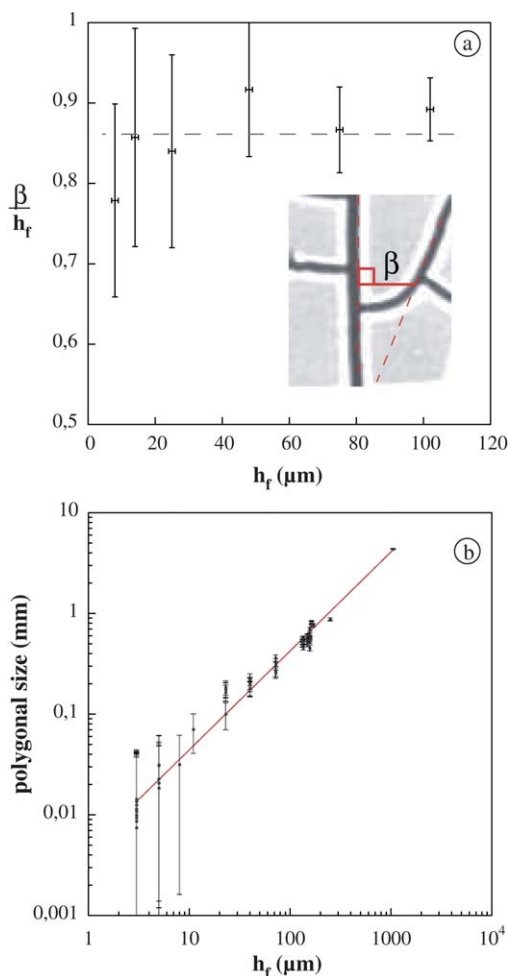


**Fig. 7** (a) Statistics on measurements of the tilting length,  $\beta$ , vs. layer thickness, characterizing the direction change of a crack due to a pre-existing one. (b) Statistics on the characteristic length of the polygonal cells (square root of the surface area) vs. layer thickness in a log–log scale. Lines are a guide for the eye.

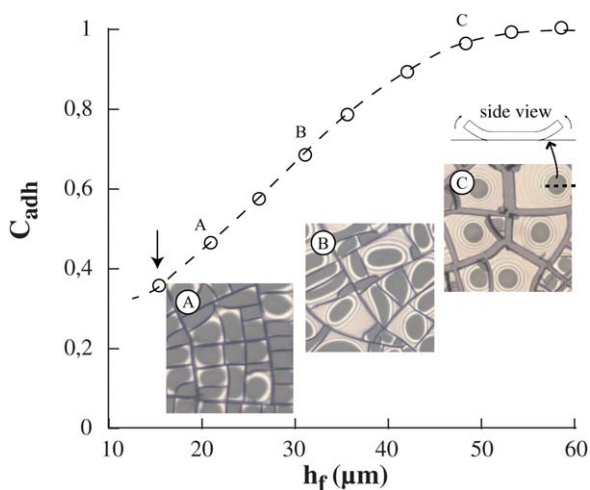


**Fig. 8** Circularity characteristic of the adhering region shape vs. final layer thickness. Inside a single cell, circular optical interference fringes encircle the adhering region (dark area). The vertical arrow shows the critical thickness leading to observable layer detachment. Dashed line is a guide for the eye.

the substrate only by a single region. In each image the adhering zone appears dark and the detached region bright. The latter is encircled by optical interference fringes due to a growing air gap between the substrate and the transparent layer (image B and C in Fig. 8). Depending on the thickness different delaminating front shapes are observed at the final stage of the delamination process. For the thinnest films ( $h_f \leq 30 \mu\text{m}$ ), the delamination process only takes place at the cell corners and close to the cell edges (image A in Fig. 8). For slightly thicker layers ( $30 \mu\text{m} \leq h_f \leq 45 \mu\text{m}$ ), adhering regions display more complex shapes (image B in Fig. 8). For thicker layers ( $45 \mu\text{m} \leq h_f$ ), the adhering regions are circular (image C in Fig. 8).<sup>20</sup>

To quantify the change in shape of the adhering region at the final stage of the delamination process, we define the circularity

$C_{\text{adh}}$  by:  $C_{\text{adh}} = 4\pi \frac{A_{\text{adh}}}{l^2}$ , where  $A_{\text{adh}}$  denotes the surface area of the adhering region and  $l$  its perimeter. A circularity value of 1 indicates a perfect circle; when the value approaches 0, it indicates an increasingly elongated shape. In our system, statistics measurements show that the circularity approaches 1 for increasing layer thickness (Fig. 8).

### 4.3 Circular and spiral cracks ( $h_s < h$ )

As the drying process persists, residual stress remains inside the adhering regions of the gel: consequently cracks can form inside these regions. Indeed observations show that a new generation of cracks form if the layer is thick enough. They propagate inside the adhering region a some time after the delamination process has finished and without observing any delamination correlated to this cracking process. The adhering regions are preferentially circular and a new crack starts at the border of the adhering region then propagates along either a circular path (Fig. 9a), or a spiral trajectory (Fig. 9b).

Differential focusing by optical microscopy allows the identification of both types of crack in the layer thickness and to verify

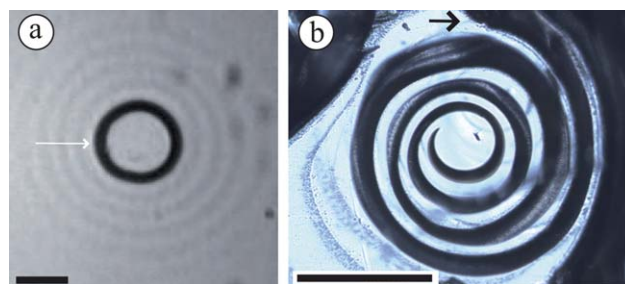


**Fig. 9** Digitized images by optical microscopy of the final crack patterns showing (a) a circular path (encircled by circular optical interference fringes) or a spiral path (b) (focused on the plane of the substrate). Both crack patterns are formed in the adhering regions. Arrows indicate the initiation of each crack. Scale bars = 100  $\mu\text{m}$ .

that (i) they lie at an oblique angle to the plane of the substrate leading to an axisymmetric cone-shape or conical spiral cracks (ii) they do not extend in the whole thickness of the layer, but from the substrate until a distance  $\Delta$  from the surface of the layer as described in the sketch in Fig. 10a. As evidence, the traces of the spiral crack on the substrate can be observed after the gelled layer has been removed (insert in Fig. 10b). Fig. 10b gives the spiral height. One can also make a rough estimation of the solvent–air menisci mean position,  $h_m(t_s)$ , at the time  $t_s$  of formation of the crack (see appendix A). The method is somewhat cumbersome also we apply it only to a small selection of points. For instance, for a typical layer thickness  $h_f = 90 \pm 3 \mu\text{m}$ , we estimate  $h_m(t_s) = 50 \pm 5 \mu\text{m}$  and  $\Delta = 33 \pm 3 \mu\text{m} \sim h_f - h_m(t_s)$ . It allows to conclude that the upper part of the crack corresponds approximately to the solvent–air menisci position at time  $t_s$ .

The spiral shape is close to an Archimedean (linear) spiral. A side view of the spiral crack is sketched in Fig. 10a. While turning, the tilt angle  $\theta$  of the planar crack slowly decreases as shown in Fig. 10b. Consequently, the planes of the crack become more and more close to being a right angle with the plane of the substrate. Also, while turning, the velocity of the crack tip decreases as shown in Fig. 10c. Fig. 4(a'', b'', c'') display a series of images taken during the propagation of a conical spiral crack. The final spiral shape is formed in about 3 min.

In some cases, either one circular crack (Fig. 9b) or two concentric circular cracks (Fig. 11) are formed. When two cracks are present the tilt angle,  $\theta$ , of the inner crack is closer to zero than for the outer one. The first crack to form is the external one, followed by the inner one. Both propagate much faster than the spiral crack, that is in less than 1/10 s. Also observations show that axisymmetric cracks occur preferentially inside an adhering region located in the center of a polygonal cell whereas spiral cracks form in adhering region off-centered in the polygonal cell. This suggests a more homogeneous mechanical stress field in the plane of the layer when the adhering region is located in the center of a polygonal cell. For illustration, Fig. 11 shows two adjacent polygonal cell, one exhibiting a conical spiral crack, the other concentric conical circular cracks inside an adhering region relative the middle of the cell.

## 5 Discussion

Cracking during drying is complex due to the coupling of time dependent consolidation and fracture problems. Qualitative

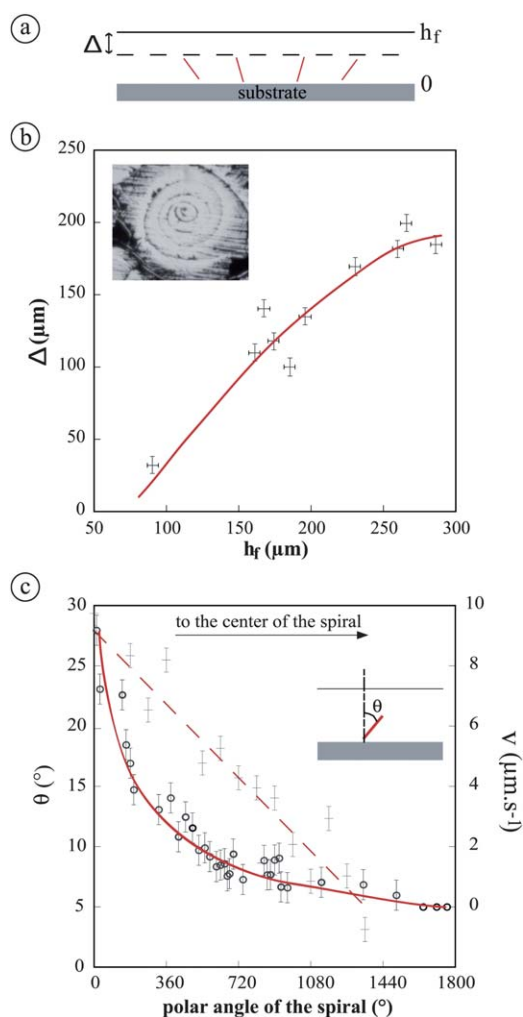


**Fig. 10** (a) Sketch showing a sectional view of a conical spiral crack. The depth of the crack extends from the substrate to a distance  $\Delta$  from the layer surface. (b) Distance,  $\Delta$ , between the layer surface and the crack position in the thickness vs. final layer thickness,  $h_f$ ; insert: trace of the spiral crack left on the substrate after the polygonal cell was removed. (c) (+) Tilt angle,  $\theta$ , to the perpendicular direction at the substrate and (○) orthoradial velocity of the crack tip,  $v$ , as a function of the polar angle. Lines are guides for the eye.

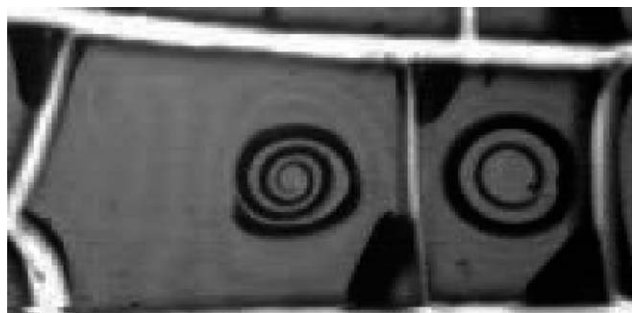


**Fig. 11** Spiral crack and concentric circular cracks in two adjacent polygonal cells. Image width is 600  $\mu\text{m}$ .

understanding of the pattern can be achieved using linear elastic fracture mechanics, but to perform quantitative comparison with experiment, it is necessary to characterize the mechanical

behavior and the loading of the porous solid matrix. Recently, some attempts<sup>11,17,28,29</sup> to do this have been made but at present no model is fully appropriate and such comparisons will be the object of a further paper. In the meantime, let us review, the different explanations that can be given for each pattern.

First, the minimum thickness  $h_C$  for cracks to appear can be understood by using the Griffith<sup>30</sup> argument: below this thickness the elastic energy stored in the film is too weak to overcome the fracture energy.<sup>18</sup> It<sup>17</sup> has been successfully applied to the drying of colloids using a stress/strain relation proposed by Routh and Russel.<sup>31</sup> We are currently working on the other critical thicknesses  $h_D$  for the apparition of the delamination and  $h_S$  for the spiral cracks. At present, to our best knowledge, no explanation for the transition  $h_C^1$  between sinuous and channelling craquelures has been given.

Concerning the crack shapes, nucleation and sinuous crack propagation have not yet been studied; also, the polygonal crack patterns have been shown to form hierarchically.<sup>26</sup> Dimensionless parameters  $\alpha_0$  and  $\alpha_1$  may serve to characterize quantitatively those patterns and an effort has to be made to link them to the material and drying conditions. Delamination clearly depends on the mismatch between cohesion of the material and adhesion to the substrate. Also the delamination process is not guaranteed to occur with every system. In the system studied here, delamination occurs from the corners due to the presence of a well-known stress singularity.<sup>32</sup> The dependence of the patterns with the relative humidity has been studied.<sup>20</sup> The tendency to become circular has been noticed in other geometries<sup>33,34</sup> but not demonstrated at present.

Spiral cracks have been observed in drying precipitates<sup>21</sup> and in other systems.<sup>35–37</sup> Some of them grow inwards<sup>21,35,36</sup> like ours, the others outwards.<sup>37</sup> The outwards propagating ones are compatible with a crack path in tensile loading (mode I) annihilating shear loading (mode II)<sup>38,39</sup> on the crack faces but not the ones propagating inwards such as ours,<sup>40</sup> at least if the crack is perpendicular to the substrate. The influence of the tilt angle  $\theta$  (Fig. 10) has not yet been investigated and may reconcile inwards propagating spirals with this view. It shall also be noticed that in our system, the spiral cracks appear some time after the delamination process has stopped, contrary to the case observed in ref. 21.

## 6 Conclusion

Using a colloidal dispersion with transparent properties until the end of the drying process, we obtained crack free films, craquelures, delamination, spiral and circular cracks by simply increasing the film thickness. Particularly we have highlighted some parameters allowing us to describe quantitatively cracking during the drying process:

- The drying rate transition time  $t_{CRP}$  between the CRP and the FRP and  $t_{end}$  of the end of the drying process.
- The critical thicknesses  $h_C$ ,  $h_C^1$ ,  $h_D$ ,  $h_S$  giving the transition between the different types of crack patterns: sinuous, channelling, delamination and spiral cracks.
- The time  $t_c$ ,  $t_d$ ,  $t_s$  of apparition of the cracks.
- The parameters  $n$ ,  $\alpha_0$  and  $\alpha_1$  respectively are linked to the number of crack generations, the tilt angle and the polygons sizes.

- The circularity  $C_{\text{adh}}$  of the delamination process.
- The tilt angle rate and velocity of the spiral cracks.

In this paper, their values are obtained as a function of the film thickness, for a given system (colloidal dispersion, substrate) under given drying conditions. Their dependence with some other parameters (particle size, evaporation rate,...) may be derived for several purposes: to assess the models, and in the absence of models to retrieve by inverse method their formation conditions, for instance in the field of engineering for expert evaluation after an accident, in geological fields for mud cracks<sup>2</sup> or septarias,<sup>3</sup> in the arts to study painter techniques<sup>4</sup> or to authenticate paintings.<sup>5–7</sup>

## Appendix: Estimation of the liquid height in the porous layer

From the experimental measurements, the mean position of the solvent–air menisci at time  $t$ ,  $h_{\text{m}}(t)$ , can roughly be estimated. Indeed, in a simplified view, one can be rewritten as:

$$m(t) = \rho_{\text{w}}A_{\text{w}}(h_{\text{f}} - h_{\text{m}}(t)) + \rho_{\text{p}}V_{\text{p}}$$

where  $A_{\text{w}}$  is the mean surface area occupied by the pores in a plane parallel to the substrate that can be estimated by the total surface area of the film multiplied by  $\phi_{\text{rcp}}$ , and  $m(t)$  the quantity of solvent removed by evaporation that is obtained by mass measurements. In this equation, all the quantities except  $h_{\text{f}}$  can be quantified so that  $h_{\text{f}}$  can be derived from it.

## References

- 1 P. Xu, A. S. Mujumdar and B. Yu, *Drying Technology*, 2009, **27**, 636–652.
- 2 L. Goehring, R. Conroy, A. Akhter, W. J. Clegg and A. F. Routh, *Soft Matter*, 2010, **6**, 3562–3567.
- 3 A. Seilacher, *Sediment. Geol.*, 2001, **143**, 41–57.
- 4 C. Lahanier, *La Joconde – Essai scientifique*, Codex Images/C12, 2008.
- 5 L. Pauchard, V. Lazarus, B. Abou, K. Sekimoto, G. Aitken and C. Lahanier, *Reflats de la Physique, Société Française de Physique*, 2007, **3**, 5–9.
- 6 S. P. Bucklow, ICOM Edinburg, 1996s.
- 7 S. L. Bucklow, *Language Resources and Evaluation*, 1997, **31**, 1572–0218.
- 8 E. R. Dufresne, E. I. Corwin, N. A. Greenblatt, J. Ashmore, D. Y. Wang, A. D. Dinsmore, J. X. Cheng, X. S. Xie, J. W. Hutchinson and D. A. Weitz, *Phys. Rev. Lett.*, 2003, **91**, 224501.
- 9 W. P. Lee and A. F. Routh, *Langmuir*, 2004, **20**, 9885–9888.
- 10 L. Pauchard, B. Abou and K. Sekimoto, *Langmuir*, 2009, **25**, 6672–6677.
- 11 G. Gauthier, V. Lazarus and L. Pauchard, *Europhys. Lett.*, 2010, **89**, 26002.
- 12 K. I. Dragnevski, A. F. Routh, M. W. Murray and A. M. Donald, *Langmuir*, 2010, **26**, 7747–7751.
- 13 L. Goehring, W. J. Clegg and A. F. Routh, *Langmuir*, 2010, **26**, 9269–9275.
- 14 A. Atkinson and R. M. Guppy, *J. Mater. Sci.*, 1991, **26**, 3869–3873.
- 15 A. Groisman and E. Kaplan, *Europhys. Lett.*, 1994, **25**, 415–420.
- 16 H. Colina and S. Roux, *Eur. Phys. J. E: Soft Matter Biol. Phys.*, 2000, **1**, 189–194.
- 17 K. B. Singh and M. S. Tirumkudulu, *Phys. Rev. Lett.*, 2007, **98**, 218302.
- 18 J. W. Hutchinson and Z. Suo, in *Mixed Mode Cracking in Layered Materials*, ed. J. Hutchinson and T. Wu, Academic Press, 1992, vol. 29, pp. 63–191.
- 19 K. B. Toga and B. E. Alaca, *Phys. Rev. E: Stat., Nonlinear, Soft Matter Phys.*, 2006, **74**, 021405.
- 20 L. Pauchard, *Europhys. Lett.*, 2006, **74**, 188–194.
- 21 Z. Neda, K.-T. Leung, J. L. and M. Ravasz, *Phys. Rev. Lett.*, 2002, **88**, 095502.
- 22 B. Espinasse, PhD thesis, Université Paul Sabatier – Toulouse III, 2003.
- 23 T. Kudra, A. S. Mujumdar, *Advanced Drying Technologies*, 2nd edition, CRC Press, 2009.
- 24 C. J. Brinker and G. W. Scherer, *Sol-gel science: the physics and chemistry of sol-gel processing*, Academic Press, Boston, 1990.
- 25 P. Coussot, *Eur. Phys. J. B*, 2000, **15**, 557–566.
- 26 S. Bohn, L. Pauchard and Y. Couder, *Phys. Rev. E: Stat., Nonlinear, Soft Matter Phys.*, 2005, **71**, 046214.
- 27 S. Bohn, S. Douady and Y. Couder, *Phys. Rev. Lett.*, 2005, **94**, 054503.
- 28 M. S. Tirumkudulu and W. B. Russel, *Langmuir*, 2004, **20**, 2947–2961.
- 29 M. S. Tirumkudulu and W. B. Russel, *Langmuir*, 2005, **21**, 4938–4948.
- 30 A. A. Griffith, *Philosophical Transactions of the Royal Society of London*, 1920, **221**, 163–198.
- 31 A. Routh and W. Russel, *Langmuir*, 1999, **15**, 7762–7773.
- 32 H. Yu, M. He and J. Hutchinson, *Acta Mater.*, 2001, **49**, 93, no.1: 93–107, 93–107.
- 33 N. Sukumar, D. L. Chopp and B. Moran, *Eng. Fract. Mech.*, 2003, **70**, 29–48.
- 34 V. Lazarus, *International Journal of Fracture*, 2003, **122**, 23–46.
- 35 B. J. Macnulty, *J. Mater. Sci.*, 1971, **6**, 1070–1074.
- 36 D. A. Dillard, J. A. Hinkley, W. S. Johnson and T. L. S. Clair, *J. Adhes.*, 1994, **44**, 51–67.
- 37 M. Sendova and K. Willis, *Appl. Phys. A: Mater. Sci. Process.*, 2003, **76**, 957–959.
- 38 R. V. Goldstein and R. L. Salganik, *Int. J. Fract.*, 1974, **10**, 507–523.
- 39 B. Lawn, *Fracture of brittle solids—Second edition*, The Press Syndicate of the University of Cambridge, Cambridge, UK, 1993.
- 40 Z. C. Xia and J. W. Hutchinson, *J. Mech. Phys. Solids*, 2000, **48**, 1107–1131.